Correcting for Reflection Attenuation in the Extreme Ultraviolet Due to Surfce Roughness

Greg Hart

A senior thesis submitted to the faculty of
Brigham Young University
in partial fulfillment of the requirements for the degree of

Bachelor of Science

Dr. R Steven Turley, Advisor

Department of Physics and Astronomy

Brigham Young University

August 2012

Copyright © 2012 Greg Hart

All Rights Reserved

ABSTRACT

Correcting for Reflection Attenuation in the Extreme Ultraviolet Due to Surfce Roughness

Greg Hart
Department of Physics and Astronomy
Bachelor of Science

We quantitatively characterized the effect surface roughness has on extreme ultraviolet radiation. This was done by taking the ratio of the reflectance of a surface with random roughness and the reflectance from a perfectly smooth surface of the same composition and size. The reflectance was calculated by numerically solving the exact integral equations for the electric and magnetic fields for s polarization. The surfaces had low spatial-frequency noise in one direction and were invariant in the other. The reflectance for the rough surface was averaged from many different random surfaces. In order to determine the parameters that affect this ratio, we varied angle of incidence, rms height of the roughness, thickness of the substance, real and imaginary parts of the index of reflection, and frequency cut-off for the random noise on the surface. We determined that in the extreme ultraviolet only the angle and rms height mattered. We did a fit to create a correction factor and compared it to Debye-Waller and Nevot-Croce correction factors.

Keywords: extreme ultraviolet, XUV, EUV, reflection, rough surface, attenuation

ACKNOWLEDGMENTS

I would like to thank my advisor Dr. Turley. His time, effort, and continuing patient made this possible for me. I will always be grateful for his example and all he has taught me, which has not been limited to this research or even the realm of physics. I would also like to thank BYU's Fulton Supercomputing Lab and Department of Physics and Astronomy for providing me with the resources and support necessary to complete this research. Lastly I would like to thank my wife, Danielle, for her abundant patience and encouragement.

Contents

Table of Contents **vii**

1 Introduction **1**
1.1 Interest in XUV 1
1.2 Roughness and Surfaces 5
1.3 Previous Work 8
1.4 Research Scope 14

2 Procedure **17**
2.1 Problem Setup 17

3 Results **19**
3.1 Results 19
3.2 Issues 22

4 Conclusion **25**
4.1 Conclusion 25
4.2 Further Work 26

Bibliography **29**

Chapter 1

Introduction

1.1 Interest in XUV

The extreme ultraviolet (XUV) is the bridge between ultraviolet and x-ray with wavelengths between one and 100 nanometers. In recent years there has been an increased interest in XUV optics. This interest arises from new applications and the possibility of realizing old applications.

For example, astronomy depends on electromagnetic radiation for virtually all of their discoveries; this means all wavelengths have the potential to contribute new understanding. XUV light can be used to observe objects such as white dwarfs and redshifts of x-ray producers [1–3]. In addition, XUV optics have recently found application in planetary science. The Earth's magnetosphere traps singly ionized helium which gives off XUV radiation. Thus, XUV light provides a way to observe the magnetosphere and how it changes over time [4, 5].

XUV optics also have applications in microchip fabrication [3, 6]. Many microchips are made by the process of photolithography. Photolithography requires exposing photosensitive material to an image of what is desired, causing it to be etched into the surface. Photolithography has been around for many years and there has been much research into getting it to produce smaller

circuits. This effort has been successful, producing several methods that allow manufactures to create features smaller then the resolution of the light they are using [7, 8]. Even with these great successes, using small wavelength light would give greater resolution allowing even smaller, and hence, faster chips.

The field of microscopy also stands to benefit from improved XUV optics [9]. Particularly, XUV offers benefits in looking at biological systems. XUV microscopes offer higher resolution than visible light microscopes and easier sample preparation than electron microscopes. There are ranges in the XUV where water is transparent and carbon is opaque [10], making it easy to see the inside of a cell without staining it or similar preparation.

Realizing all of these applications require making improvements to XUV optics. Making optics begins with understanding how the light interacts with material. When light impinges on a surface, energy must be conserved. Therefore we have to be able to account for all the energy of the incoming beam. After the interaction the energy is distributed between reflection, transmission, and absorption. How the energy is distributed is dependent on the complex index of refraction, a frequency-dependent property of the material

$$\mathscr{N} = n + i\beta \tag{1.1}$$

where n is the real part of the index of refraction and β is the imaginary part [3]. The imaginary part of the index represents the absorption of the material. Both the real and imaginary parts of the index are used to determine the reflected and transmitted portions of the light. The index of refraction becomes the key to predicting how optics behave. Therefore BYU's XUV group has spent a lot of time to determine the index of refraction for different materials [11, 12].

Arbitrary light can be broken into two components or polarizations. The most common polarizations to use are s and p (see figure 1.1). S polarization (s stands for *senkrecht*, the German word for perpendicular) is the part of the light whose electric field oscillates perpendicular to the plane of incidence (the plane that the incident and reflected light are in). P polarization (p stands for *par-*

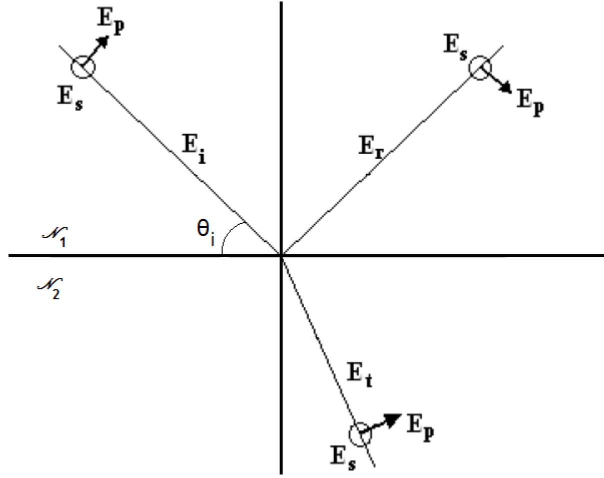

Figure 1.1 The geometry of s and p polarization. The plane of the page is the plane of incidence.

allel, the German word for parallel) is the component whose electric field oscillates in the plane of incidence. Since the electric field must be perpendicular to the direction of propagation, these two polarizations are linearly independent, forming a basis for any problem. Also as we introduce roughness we will assume that the surface is invariant perpendicular to the plane of incidence. This ensures (with reasonable intensities) that the two polarizations are noninteracting. Allowing the vector problem to be split into two uncoupled scalar problems.

With the light broken into components one can calculate what happens when it encounters an interface between surfaces. This is done using the electromagnetic boundary conditions. The reflected and transmitted fields for each polarization can easily be calculated for an infinite flat abrupt interface. Taking the ratio of these fields with the incident field gives the Fresnel coefficients [13]. For the reflected s and p polarizations the coefficients are respectively

$$r_s = \frac{E_r^s}{E_i^s} = \frac{\mathcal{N}_1 \sin\theta_i - \sqrt{\mathcal{N}_2^2 - \cos^2\theta_i}}{\mathcal{N}_1 \sin\theta_i + \sqrt{\mathcal{N}_2^2 - \cos^2\theta_i}} \tag{1.2}$$

and

$$r_p = \frac{E_r^p}{E_i^p} = \frac{\mathcal{N}_1 \sqrt{\mathcal{N}_2^2 - \cos^2\theta_i} - \mathcal{N}_2^2 \sin\theta_i}{\mathcal{N}_1 \sqrt{\mathcal{N}_2^2 + \cos^2\theta_i} + \mathcal{N}_2^2 \sin\theta_i} \tag{1.3}$$

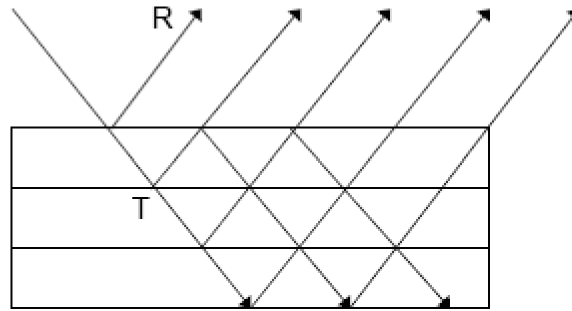

Figure 1.2 An illustration of reflections from a multilayer mirror.

where $\mathscr{N}_1$ is the index of the material the light is coming from, $\mathscr{N}_2$ is the index of the material it is entering, and θ_i is the angle of the incident field measured from grazing (see figure 1.1). These coefficients can be applied to the incident field to get the reflected field (including any phase shift) or by squaring the magnitude we can get a coefficient for the reflected intensity

$$R_s = |r_s|^2 \tag{1.4}$$

and

$$R_p = |r_p|^2. \tag{1.5}$$

In the XUV range the real part of the index of refraction is close to one. The imaginary part of the index of refraction is larger then zero. These general properties of the index of refraction mean that materials are highly absorptive and poor reflectors. This is one of the difficulties in building good XUV optics. In order to strengthen the reflected intensity, multilayer thin film mirrors are used (see figure 1.2). If the layers are the right thickness the reflection at each interface will constructively interfere with the others building a stronger reflection, however because of the absorption, the layers should be as thin as possible. The problem of poor reflectance is further compounded by the small wavelength of XUV light. A surface that looks perfectly flat to the eye has all sorts of imperfection that are on the scale of the small wavelengths of XUV light.

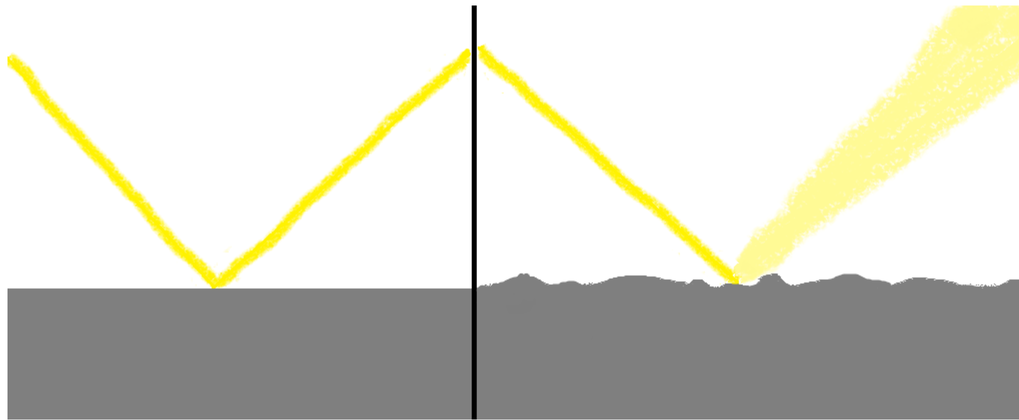

Figure 1.3 On the left is an example of perfect specular reflection. The right shows the diffuse (or nonspecular) reflection results from mild imperfections in the surface.

1.2 Roughness and Surfaces

The derivation of the Fresnel coefficients assumes a perfectly flat infinite surface, so all the reflected light is reflected at the same angle, known as the specular angle. When the surface is not flat, the light is reflected at the range of angles instead of just the specular angle (see figure 1.3). This nonspecular reflection is responsible for the observed decrease in reflected intensity.

To improve XUV optics it necessary to quantitatively understand how the surface roughness attenuates the reflected intensity. The most common way to handle surface roughness is applying a scalar correction factor [14, 15]:

$$R = R_0 C \tag{1.6}$$

where R is the measured reflected intensity, R_0 is the calculated reflected intensity off of a flat surface, and C is the correction factor. This correction factor can be a function of many things: properties of the material such as the index of refraction, the RMS roughness height of the surface, the wavelength of light, the angle of incidence, etc. The most commonly used correction factors are Debye-Waller or Nevot-Croce [16, 17]. They have the same form and are respectively

$$R = R_0 e^{-4q^2h^2} \tag{1.7}$$

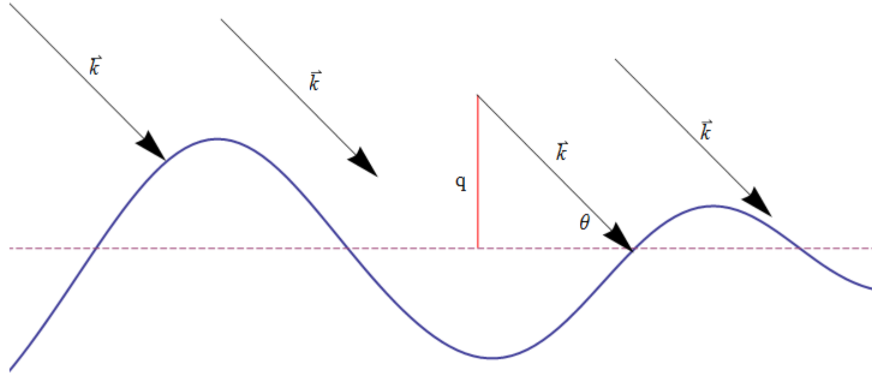

Figure 1.4 Here is the geometry of the surface. The dashed line represents the corresponding flat surface. The solid line is the actual surface. The arrows represent the wave vector of the incoming light. θ is the angle the incoming light makes with the flat surface and q is the component of the light's momentum perpendicular to the flat surface.

and

$$R = R_0 e^{-4q_1 q_2 h^2} \tag{1.8}$$

where h is the RMS height, and q is the component of the momentum perpendicular to the flat surface (see figure 1.4). Thus q is

$$\frac{2\pi\mathcal{N}}{\lambda_0}\sin\theta \tag{1.9}$$

where θ is the incidence angle from grazing, λ_0 is the wavelength in vacuum, and $\mathcal{N}$ is the index of refraction. For the Debye-Waller factor q is evaluated on one side of the interface. The Nevot-Croce factor is a modification of Debye-Waller in which q is evaluated on each side of the interface. Each produces accurate results for different angle ranges, but neither accurately covers a large range of angles [18].

They both rely on the assumption that the rough surface is made from Gaussian noise around the flat surface. We hope that using a more realistic surface model will produce a similar but more accurate correction factor, applicable across a larger range of angles. This requires knowledge

of what real surfaces look like. Our mirrors are created through the processes of sputtering or evaporation. Depending on the details of the process (temperature, thickness, materials, annealing conditions, etc.) the atoms have a degree of randomness in their locations. In most cases, there is a tendency for the formation of locally ordered structures which removes some of this randomness resulting in no big jumps or discontinuities in the surface. In most models, surface roughness is characterized by the root mean square (RMS) height. Modeling the surface as heights with a Gaussian distribution having a given RMS height can make the surface unrealistically jagged. A more realistic way to produce the surface would be to have widely-spaced points whose height is determined by a random Gaussian distribution giving the desired RMS height. Then the rest of the surface is produced by smoothly connecting these points with a spline. The spatial-frequency of this surface can be partially controlled by changing the number, and hence the spacing, of the random points. To validate our surface models, Alex Rockwood examined several samples using atomic force microscopy (AFM) [19]. This confirmed that the surfaces do have roughness but it is closer to rolling hills than jagged rocks (see figure 1.5). He took a Fourier transform of the surface. This revealed that real surfaces have low spatial frequencies. Observations of the spline method in frequency space revealed that it did not consistently give spectrums similar to real surfaces. Therefore in order to better represent real surfaces a frequency filter is used [20]. Surface points are generated by the random Gaussian distribution, after which its Fourier transform is sent through a low pass Gaussian filter whose standard deviation is controlled by a parameter called the frequency cut-off (ω). This makes almost 70% of the frequencies smaller then ω. After the low pass filter, if one is cautious with the phases, they can transform back to real space and get a low spatial-frequency surface[1] (see figure 1.5).

In the 1994 de Boer derived a more general correction factor that reduces to Debye-Waller and

[1]Making changes to the values in frequency space removes the garentee that the inverse transform will return all real values. Thus after the filter is applied we can not just apply the inverse transform.

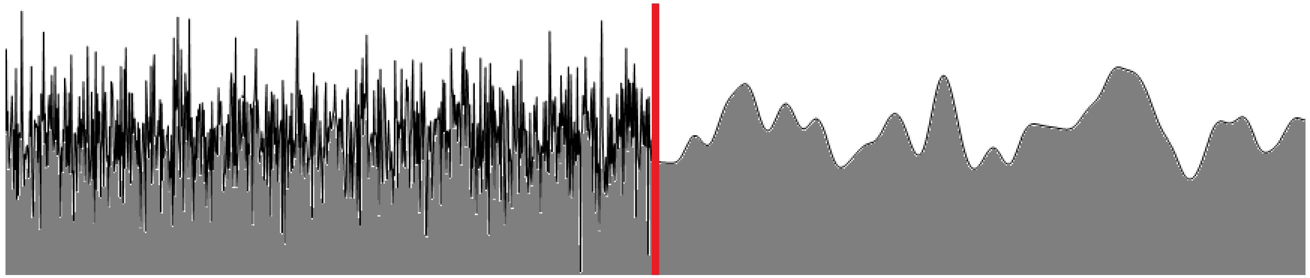

Figure 1.5 Each side is 50 wavelengths of a surface. The left side is a surface made with random Gaussian noise. The right show the surface after the low pass filter is applied leaving only the low frequencies from the noise.

Nevot-Croce in the angle ranges were each is most accurate and smoothly fills in the gap between them [18]. His factor added an additional parameter representing the lateral length correlation. This length correlation could be used to produce the low spatial frequencies found in real surfaces. David Sterns also worked on the problem of reflections off non-ideal surfaces [21]. He developed a general method for calculating the reflectance from any type of nonideal interface. Both de Boer and Stearns' derivations approximate the surface roughness as a perturbation of the smooth surface and calculate the reflectance to first order. Stearns specifically assumes the reflections are weak. Since our goal is to strengthen the reflectance this assumption may fail. Also we believe we can do better than first order and understanding how each polarizations is affected has its place.

1.3 Previous Work

In order to find a correction factor we need the ratio of rough surface reflections to flat surface reflections for many different surfaces at a large ranges of angles. To obtain this this data Jed Johnson produced a program that very accurately calculates the reflectance from a rough surface [22]. The problem is approached as a scattering problem with the surface, as mentioned earlier, being invariant in one direction reducing the problem to two dimensions (see figure 1.6). Also for simplicity he assumed that the material is nonmagnetic, i.e. $\mu = \mu_0$. The total electric field is equal

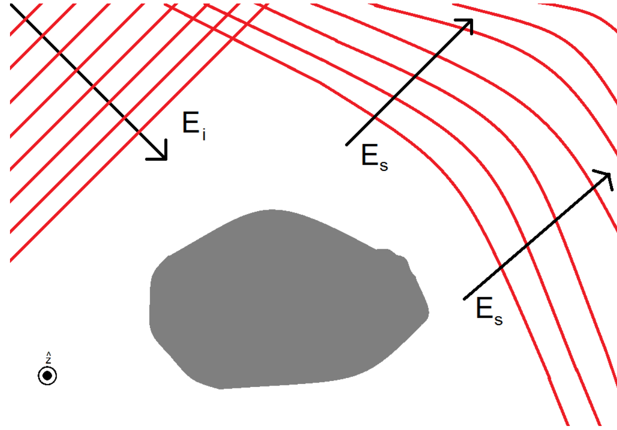

Figure 1.6 The incident (E_i) and scattered (E_s) fields. The gray represents the object causing the scattering. It is invariant in the $\hat{z}$ direction. So only what is in the plane of the picture matters.

to the incident field plus the scattered field

$$\vec{E} = \vec{E}_i + \vec{E}_s. \tag{1.10}$$

The incident field is determined by the known initial conditions. The scattered field is produced by currents induced on the scatterer by the incident field. Assuming the fields have harmonic time dependence $e^{-i\omega t}$, the familiar Maxwell equations can rewritten in the symmetric form

$$\nabla \cdot (\varepsilon_0 \vec{E}) = \rho_e \tag{1.11}$$

$$\nabla \cdot (\mu_0 \vec{H}) = \rho_m \tag{1.12}$$

$$\nabla \times \vec{E} = i\omega\mu_0 \vec{H} - \vec{K} \tag{1.13}$$

$$\nabla \times \vec{H} = -i\omega\varepsilon_0 \vec{E} + \vec{J} \tag{1.14}$$

where $\vec{H}$ is the auxiliary field, $\vec{B} = \mu \vec{H}$ and

$$\rho_e = \varepsilon \vec{E} \cdot \nabla \left(\frac{\varepsilon_0}{\varepsilon} \right) \tag{1.15}$$

$$\rho_m = \mu \vec{H} \cdot \nabla \left(\frac{\mu_0}{\mu} \right) \tag{1.16}$$

$$\vec{K} = -i\omega(\mu - \mu_0)\vec{H} \tag{1.17}$$

$$\vec{J} = -i\omega(\varepsilon - \varepsilon_0)\vec{E} \tag{1.18}$$

Having both electric and magnetic sources make the equations symmetric so the process of solving for the electric field is identical to the one for the magnetic field. Therefore I will only show equations for the electric field in the remainder of this discussion. Also note that these sources represent bound soucres.

The incident field is source free and combining Maxwell's equations gives the vecter Helmholtz equation:

$$(\nabla^2 + k^2)\vec{E}_i = 0 \tag{1.19}$$

where $k^2 = \mu\varepsilon\omega^2$. Solving for the associated Green's function

$$G(r,r') = \frac{i}{4}H_0^{(1)}(k|r-r'|) \tag{1.20}$$

where the primed coordinates are the source points, the unprimed coordinates are the observation points (see figure 1.7), and $H_0^{(1)}$ is a Hankel function of the first kind. The scattered field has sources but Maxwell's equations can likewise be combined to get

$$(\nabla^2 + k^2)\vec{E}_s = \nabla\left(\frac{\nabla\cdot\vec{J}}{i\omega\varepsilon_0}\right) - i\omega\mu_0\vec{J} + \nabla\times\vec{K} \tag{1.21}$$

which looks like the Helmholtz equation but with sources. In fact the Green's function from the Helmholtz equation can be used to solve for $\vec{E}_s$. Right multipling by the Green's function and integrating over the scatterer gives

$$\vec{E}_s = -\nabla\left(\frac{\nabla\cdot\int\vec{J}G\,da'}{i\omega\varepsilon_0}\right) + i\omega\mu_0\int\vec{J}G\,da' - \nabla\times\int\vec{K}G\,da' \tag{1.22}$$

which is the scattered field in terms of the induced currents $\vec{J}$ and $\vec{K}$. This can be written more compactly as

$$\vec{E}_s = -\frac{\nabla(\nabla\cdot\vec{A}) + k^2\vec{A}}{i\omega\varepsilon_0} - \nabla\times\vec{F} \tag{1.23}$$

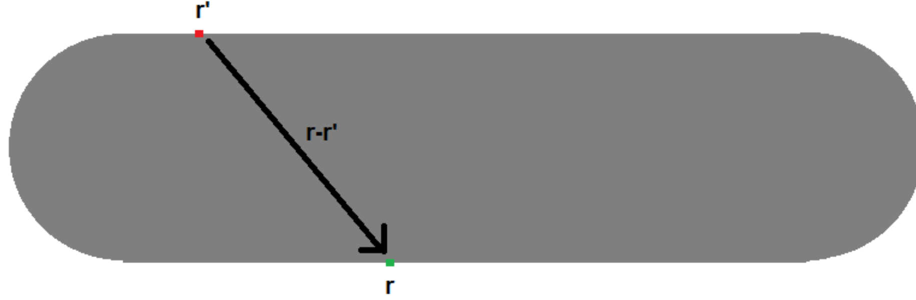

Figure 1.7 Illustration of source and observation points. The red box represents a point on the mirror where there is some surface currents creating fields (source point). The green box represents a point on the surface that is feeling or observing the effects of these fields (observation point). We will have currents all around the surface of the mirror so r' will be evaluated at every point on the surface. Also for each value of r', r will be evaluated at every point on the surface.

where the new potentials $\vec{A}$ and $\vec{F}$ have bene defined:

$$\vec{A} = \int \vec{J}(r')G(r,r')da' \tag{1.24}$$

$$\vec{F} = \int \vec{K}(r')G(r,r')da'. \tag{1.25}$$

However since the medium is assumed to be homogenous there are on bound currents in the bulk of the material. The only sources are surface currents. This reduces these integrals over the whole scatterer to integrals over its surface (line integrals in this two dimensional setup).

With this the scattering equation can be written (1.10) as

$$\vec{E} = \vec{E}_i - \frac{\nabla(\nabla\cdot\vec{A}) + k^2\vec{A}}{i\omega\varepsilon_0} - \nabla\times\vec{F}. \tag{1.26}$$

Now taking advantage of polarization. The electric field equation (1.26) is used to solve for s polarization and the corresponding magnetic field equation,

$$\vec{H} = \vec{H}_i - \frac{\nabla(\nabla\cdot\vec{F}) + k^2\vec{F}}{i\omega\mu_0} + \nabla\times\vec{A}, \tag{1.27}$$

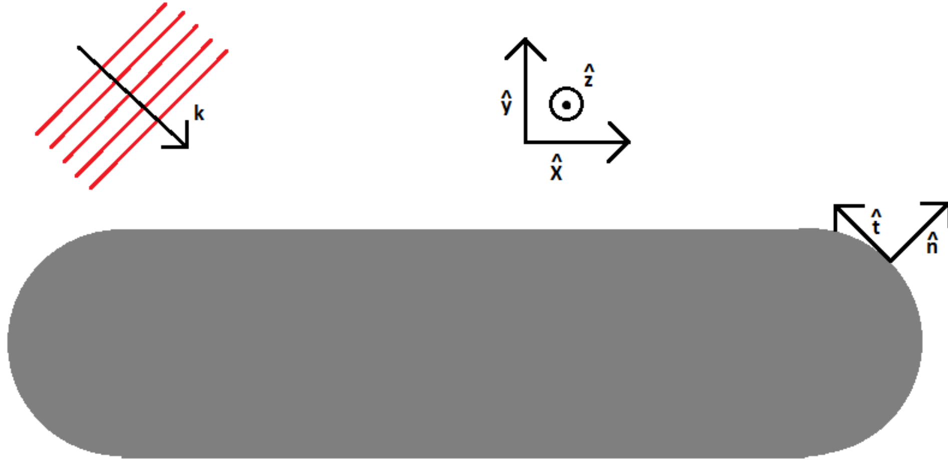

Figure 1.8 This figure shows how the coordinates are set up [22]. With z being the invariant axis. The white area is vacuum, the gray area is the mirror, and the red is the incident wave. Where $\hat{n}$ points outward and the direction of $\hat{t}$ is defined so that $\hat{n} \times \hat{t} = \hat{z}$.

to solve for p polarization. Again the method of solving the electric and mangentic equations are identical. Continuing with only the electric equation, the s polarization corresponds to the z axis (see figure 1.8). This allows us to use the z components instead of the full vectors. Since the surface is invariant along the z axis the divergence of $\vec{A}$ is 0 and we can explicitly write out the curl of $\vec{F}$. Also solving for the incident field we have

$$(E_i)_z = E_z + \frac{k^2 A_z}{i\omega\varepsilon_0} + \left[\frac{\partial F_y}{\partial x} - \frac{\partial F_x}{\partial y}\right]. \tag{1.28}$$

The last thing we need to know is that the surface currents can be written in terms of the total field

$$\vec{J} = \hat{n} \times \vec{H} \tag{1.29}$$

$$\vec{K} = \vec{E} \times \hat{n}. \tag{1.30}$$

Since the z component of $\vec{E}$ is perpendicular to $\hat{n}$ it is equal to the tangential component of $\vec{K}$. Finally we are left with an equation for the electric field. Outside of the material we have

$$(E_i)_z = K_t + \frac{k_0^2 (A_0)_z}{i\omega\varepsilon_0} + \left[\frac{\partial (F_0)_y}{\partial x} - \frac{\partial (F_0)_x}{\partial y}\right] \tag{1.31}$$

where I have added subscripts to k, A, and F to indicate that they use the permittivity of free space. Inside the material we have

$$0 = -K_t + \frac{k^2 A_z}{i\omega\varepsilon} + \left[\frac{\partial F_y}{\partial x} - \frac{\partial F_x}{\partial y}\right] \tag{1.32}$$

where E_i is 0 inside the material, K_t picks up a negative sign because the direction of normal flips, and I have dropped the subscripts because everything relies on the constants of the material. Now we have equations for the incident field in terms of the surface currents, but we know the incident field and want the scattered field. Since the currents produce the scattered field we can use these equations to solve for the currents and thus the scattered field. The only problem is that the currents are under the integrals in A and F so it has to be solved numerically.

Numerically solving an integral amounts to changing the integral to a sum of the function being integrated, where the sum is over different points at which the function is evaluated. In our case the integrals are the potentials A and F so the functions being integrated are the surface currents multiplied by the Green's function (evaluated at primed coordinates). How you go about replacing the integral with a sum (i.e. a quadrature rule) imposes an approximation on the function. For example the easiest rule is literally replacing the integral sign with a sum and changing the dx to the distance between points. This approximates the function as a series of flat steps. We used a third order rule, meaning it is exact for any function that is a polynomial of order 3 or less. This gives us

$$\begin{aligned} E_i &= K + \frac{k_0}{4\omega\varepsilon_0}\sum_j c_j S_j J(r'_j) H_0^{(1)}(k_0|r - r'_j|) \\ &+ \frac{ik_0}{4}\sum_j c_j S_j K(r'_j)\frac{H_1^{(1)}(k_0|r - r'_j|)}{|r - r'_j|}\left[\cos(\theta'_j)(y - y'_j) - \sin(\theta'_j)(x - x'_j)\right] \end{aligned} \tag{1.33}$$

where the c_js are the weights from the quadrature rule, S_j is the Jacobian, and everything else in the last term came from the derivatives and geometry of the cross product. Now to finish it off the unprimed variables need to be evaluated at specific points. This is done using the Nystrom Method, which uses the same points for the unprimed variables as those used for the integrals

(primed variables). This gives a system of equations

$$\begin{aligned} E_i(r_k) &= K(r_k) + \frac{k_0}{4\omega\varepsilon_0}\sum_j c_j S_j J(r'_j) H_0^{(1)}(k_0|r_k - r'_j|) \\ &+ \frac{ik_0}{4}\sum_j c_j S_j K(r'_j) \frac{H_1^{(1)}(k_0|r_k - r'_j|)}{|r_k - r'_j|}\left[\cos(\theta'_j)(y_k - y'_j) - \sin(\theta'_j)(x_k - x'_j)\right]. \end{aligned} \tag{1.34}$$

Now the integral with K has a singularity that needed to be treated with more care then I have done here, but when done right it only changes K by $\frac{1}{2}$. Which yields a matrix equation

$$\begin{pmatrix} \mathbf{E} \\ \mathbf{0} \end{pmatrix} = \begin{pmatrix} \mathbf{N}_0 + \frac{\mathbf{I}}{2} & \mathbf{M}_0 \\ \mathbf{N} - \frac{\mathbf{I}}{2} & \mathbf{M} \end{pmatrix} \begin{pmatrix} \mathbf{K} \\ \mathbf{J} \end{pmatrix} \tag{1.35}$$

where $\mathbf{I}$ is the identity matrix and $\mathbf{M}$ and $\mathbf{N}$ represent matrices with the coefficients of their respective currents from (1.34) and the subscripts indicate which constants to use. This type of equation (1.35) can be solved by any linear algbra software package. We can choose how accurately to calculate the currents by how finely the surface is discretized.

1.4 Research Scope

The overall goal of this research is to developed an empirical correction factor that is more accurate than Debye-Waller or Nevot-Croce and covers a larger range of angles and also is more applicable and easier to use then Stearns' or de Boer's methods. In order to accomplish this Johnson's scattering model was used to produce reflectance data. With the large amounts of data for this research a faster way of running the model was necessary. The code was changed from MATLAB to compiled FORTRAN. This increased its speed by about 100 times. It was also moved onto BYU's supercomputer. In addition to running faster, on the supercomputer we can use multiple processors to run several data sets at the same time. It also offers more memory allowing for larger data sets and modeling larger mirrors.

Once the model was running correctly on the supercomputer we could start looking at what parameters effects the reflection. The parameter's effects were determined by varying one parameter at a time and comparing the difference. In the interest of accuracy for each set of parameters the reflectance was averaged over many surfaces with different random roughness. With the parameters making the biggest difference identified, the data was fit with those parameters as the variables. This gave the correction factor valid in the XUV range.

Chapter 2

Procedure

2.1 Problem Setup

Our model of the mirror breaks it up into four surfaces: top, bottom, and two sides (see figure 2.1). The two sides are represented as semicircles whose diameters equal the thickness of the mirror. The line integrals in (1.26) require the surface to be continuous; the sides are necessary to continuously connect the top and bottom surfaces. If the surface is not continuous the surface currents develop singularities[1]. Aside from introducing numeric difficulties, these singularities physically mean large amounts of charges are building up, which is unrealistic for our mirrors. Since we are interested in thin film mirrors the sides have a small affect on reflections and their affect mostly shows up in the diffraction pattern. The bottom surface is important in multistack mirrors, but since this research is interested in the attenuation of reflections due to surface roughness the bottom surface is unimportant. Accordingly we made the bottom surface flat and normally had the absorption high so very little light would reflect off the bottom and make it make to the top of the mirror. The top surface is the one the light impinges on and hence is the one that we are studying.

[1]The first derivative also needs to be continuous. Fulfilling both of these requirements has proved difficult, and there is still room for improvement in generating the surfaces.

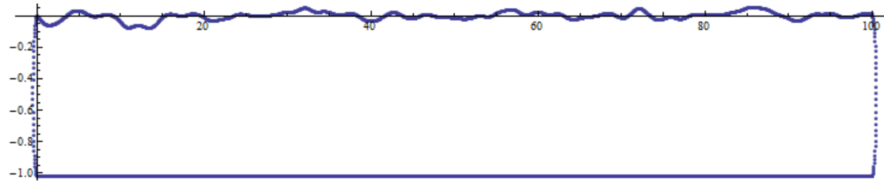

Figure 2.1 This is an example surface. Both axes are in units of wavelength but the aspect ratio is not 1:1. The surfaces are very long and skinny. The ends are semi-circles even though they look almost flat in this figure. The bottom is flat and the top has rms height of 0.1 wavelengths.

We are setting the mirrors to be long and skinny. They are typically 100 wavelengths long and generally about a wavelength thick.

Using the algorithm developed by Johnson (see section 1.3) and BYU's supercomputer we were able to calculate data for large numbers of random surfaces. Our goal was to determine what parameters significantly affected the reflectance and then to create a fit with those parameters as variables. So far we have only used the s polarization. Since the correction factor is equal to the ratio of the measured (rough surface) reflectance to the theoretical (flat surface) reflectance we also calculated the reflectance from a flat surface with the same parameters and output the ratio. The ratio was specifically of the peak intensities. We used peak intensities because in our experimental setup the detector is narrow. However these results may not be valid for a larger detector that may get extra intensity from side lobes or a boarder main lobe. Each set of parameters were used for 100 different random rough surfaces. After taking the ratio of reflectance the mean was calculated. We explored the affects of mirror thickness, frequency cut-off, and the real and imaginary parts of index of refraction. Each was viewed at a range of incident angles and rms roughnesses.

Chapter 3

Results

3.1 Results

Since we anticipate that our correction factor will have the same form as Debye-Waller and Nevot-Croce and in order to better compare them, rather than plotting and fitting the ratios of reflectance we use the negative natural log of the ratio $(-\ln(\frac{R}{R_0}))$. Thus we are finding and looking at the exponent of the correction factor. This means that on the graphs moving in the positive y direction means more attenuation of the reflectance. Also since our surface is invariant along the z axis we do not get scattering in that direction. While a real surface has scattering in both directions. However the roughness will not have a preferred direction so the attenuation should be the same for both dimensions. Putting both direction together put a factor of $\sqrt{2}$ in the exponent. With this added factor we can truly compare our correction factor with Debye-Waller and Nevot-Croce.

As we varied the different parameters we used the following for the parameters that remained constant: the imaginary part of the index of refraction was 5. This caused high absorption so that there was little affect from the back side of the mirror allowing us to focus on what happens on the top surface. The real part of the index was 0.9, since n is close to one for materials in the XUV. The

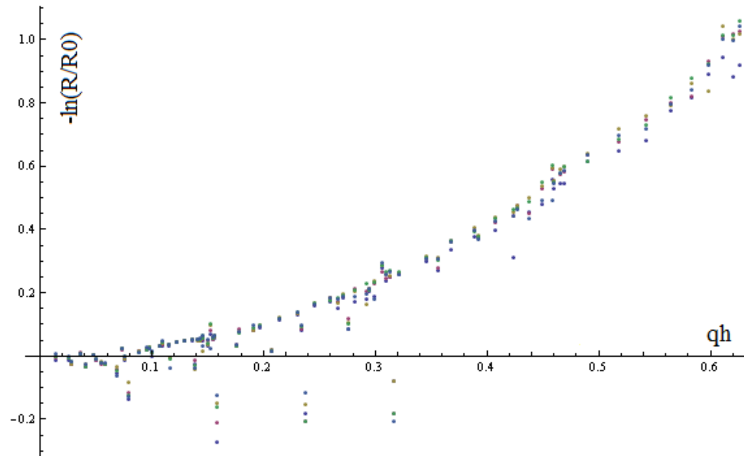

Figure 3.1 A plot of the -ln($\frac{R}{R_0}$) for varying frequency cut-offs on the Gaussian noise (ω). Five cut-offs from $\omega = 0.2$ to $\omega = 0.05$ inverse wavelengths. For each cut-off value the reflectance ratio was calculated at 80 difference values of qh. It appears to follow a parabola.

thickness of the mirror was about 1 wavelength. The frequency cut-offs were 0.1 and 0.2 inverse wavelengths. The rms height varied from 2.5% to 10% of a wavelength and the angle from 5°to 85°.

The first parameter we tested was the width of the Gaussian filter used to cut-off the frequency of the noise. We used frequency cut-offs from 0.05 inverse wavelengths to 2 inverse wavelengths. For the higher frequencies (2 to 0.2 inverse wavelengths), the ratio of the reflectance varied significantly as the cut-off frequency changed. However, as mentioned earlier, surfaces of actual XUV mirrors do not have high frequency noise and these frequencies (2 to 0.2 inverse wavelengths) are above what was observed to be realistic [19]. When examining only results from surfaces with a frequency cut-off of 0.2 inverse wavelengths or lower there was much less spreading in the reflectance ratio (see figure 3.1). As long as the frequency cut-off is below 0.2 inverse wavelengths, which it usually should be to model real surfaces, it causes little variation in the ratio of reflectance. However at the shorter end of our wavelength range the spatial-frequencies climb above this and start having greater effects. Accordingly further research into the effect of the spatial-frequency

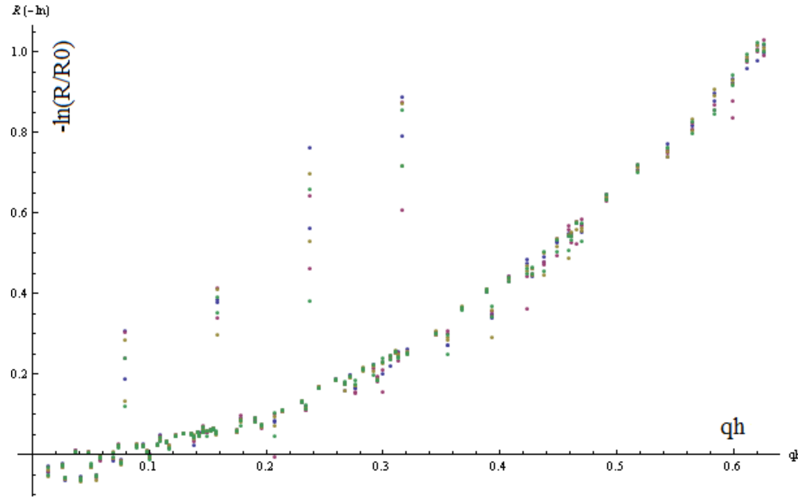

Figure 3.2 A plot of the -ln($\frac{R}{R_0}$) for varying real part of the index of refraction (n). Six values of n from $n = 0.1$ to $n = 0.92$. For each n value the reflectance ratio was calculated at 80 difference values of qh. It appears to follow a parabola.

would allow the surface roughness to be characterized by a parameter that is a function of both rms height and spatial-frequency.

The next parameter tested was the index of refraction. The difference between Debye-Waller and Nevot-Croce is how the index of refraction affects the attenuation of the reflectance. Does the index from the second material matter or just the index of the first material (vacuum in our case)? When finding the reflectance from a flat surface, the index of refraction plays a role because it appears in the Fresnel coefficients. By taking the ratio of the reflectance of the rough surface and the flat surface, the Fresnel coefficients cancels and thus the effect of index disappears. Since in our model we are always coming from vacuum we can vary the index of refraction of the mirror and determine if both indexes are needed when correcting for roughness.

We started by varying the real part of the index of refraction (n). We used values of n from 0.1 to 0.92. In the XUV $n \approx 1$ for most materials. So this range of values extends beyond what we expect to encounter. The spread of the reflectance ratios is very narrow (see figure 3.2) . In fact the spread in our ratios is smaller then the difference between Debye-Waller and Nevot-Croce for a

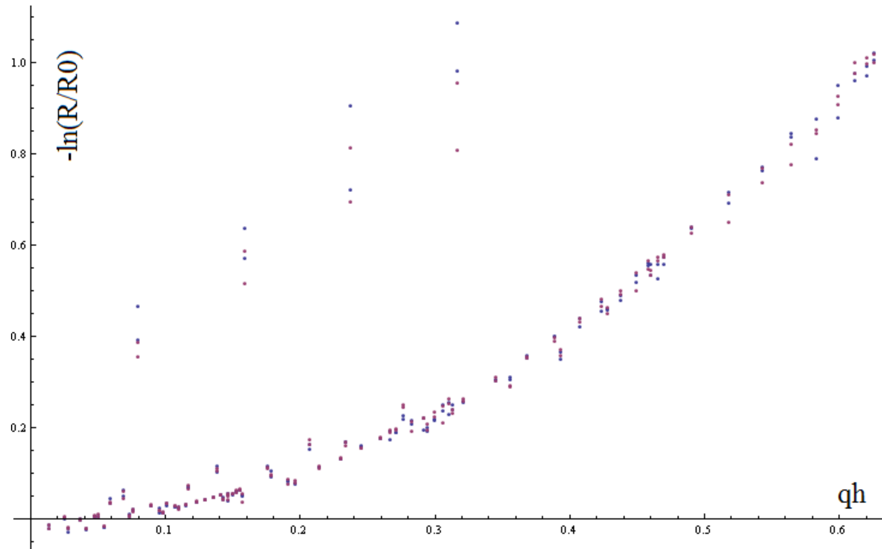

Figure 3.3 A plot of the -ln($\frac{R}{R_0}$) for varying imaginary part of the index of refraction (β). Six values of β from $\beta = 0.01$ to $\beta = 15$. For each β value the reflectance ratio was calculated at 80 difference values of qh. It appears to follow a parabola.

single n. This shows that, at least for the real part, the index of the second material does not matter. So having a single q, as the Debye-Waller factor does, looks promising.

Next we explored the affect of the imaginary part of the index of refraction (β). We varied β from 0.01 to 15. While XUV materials tend to be very absorptive this range going higher than what we expect to encounter. For the values of $\beta \leq 1$ there was significant interference from the bottom surface. However as we increase β beyond one, this interference drops off and we find that β has little affect on the change in reflectance (see figure 3.3). Combining this with the results from the real part of the index we can conclude that attenuation in the reflection caused by roughness is independent of the complex index of the material from which it is reflected.

3.2 Issues

As can be seen in the previous figures (3.1, 3.2, and 3.3) there are always several values of qh for which the reflectance ratio greatly differs from the values of the neighbors. Examining these

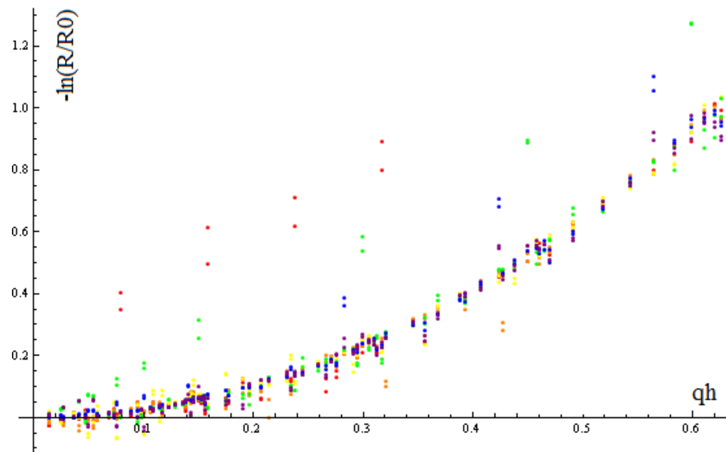

Figure 3.4 A plot of the -ln($\frac{R}{R_0}$) for varying thickness of the mirror (t). Six thicknesses from $t = 1$ to $t = 10$ wavelengths. For each thickness the reflectance ratio was calculated at 80 difference values of qh.

qh values we found that they all have the same incident angle. Thinking that these spikes arose from interference with the back surface we also explored the affect of thickness on the reflectance. We varied the thickness for 1 to 10 wavelengths, making sure to use thicknesses that were both an integer number and irrational number of wavelengths. Unsurprisingly the location of these spikes change with thickness (see figure 3.4), showing dependence. However, when the thickness is changed by an integer multiple, the spike–surprisingly–does not move back to where it started; which is expected if it were due to interference from the back surface. We run over a smaller angle range, centered on the spike, with higher resolution and found that the spike is not at a single point but is a small oscillation (see figure 3.5).

Calculating the reflection off a flat surface for a large range of angles for each incident angle revealed that in addition to getting a strong specular reflection there was always some reflection at the angle of the spike. This same nonspecular reflection at a fixed angle does not show up with the rough surfaces leading to the sudden change in reflection attenuation. This nonphysical behavior lead to the discovery that the matrix in (1.35) is not well conditioned. Particularly the eigenvalues around the problematic angle are close to zero. We are still seeking for the best fix for this problem

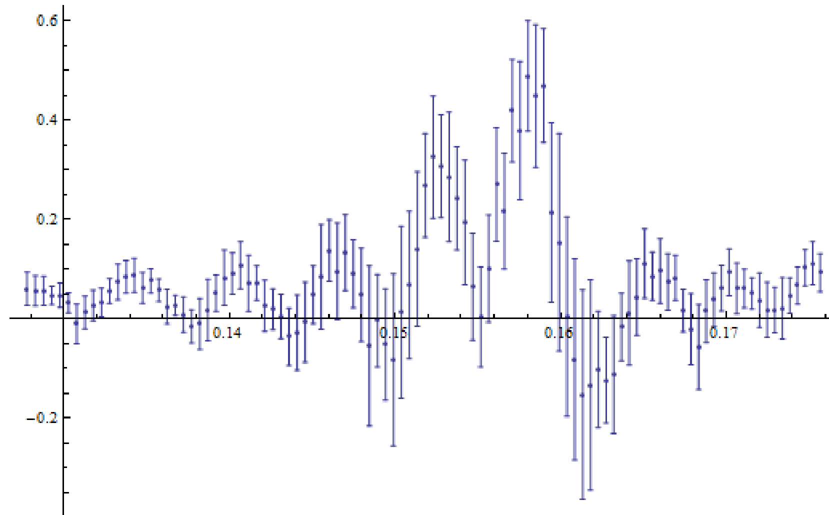

Figure 3.5 A plot of the -ln($\frac{R}{R_0}$) over an angular range of 24 to 34 degrees with a fixed h and angular resolution of 0.1 degrees.

(see Section 4.2), but in the mean time I throw out the data near the problematic angle before doing anything with the data.

Chapter 4

Conclusion

4.1 Conclusion

To find the correction factor we fit the data from varying the cut-off frequency to a third order polynomial. We assumed that the constant term was zero because when qh is zero either the surface is flat ($h = 0$) or we are just grazing the surface ($\theta = 0$) and then roughness should have no effect. From the fit we have

$$-0.28qh + 3.58(qh)^2 - 0.87(qh)^3$$

where the errors on the coefficients are 6%, 33%, and 39% respectively. This gives an overall correction factor of

$$e^{0.28qh - 3.58(qh)^2 + 0.87(qh)^3}.$$

While this is similar to Debye-Waller it exhibits smaller decreases in the reflection (see figure 4.1).

We found that this factor does depend on the rms roughness and angle of incidence. We also looked for correlations with index of refraction, and spactal frequency. However no correlation was discovered and if these parameters are kept within realistic ranges for the XUV, their affect on the reflectance is small compared rms height and incident angle. While our correction factor is

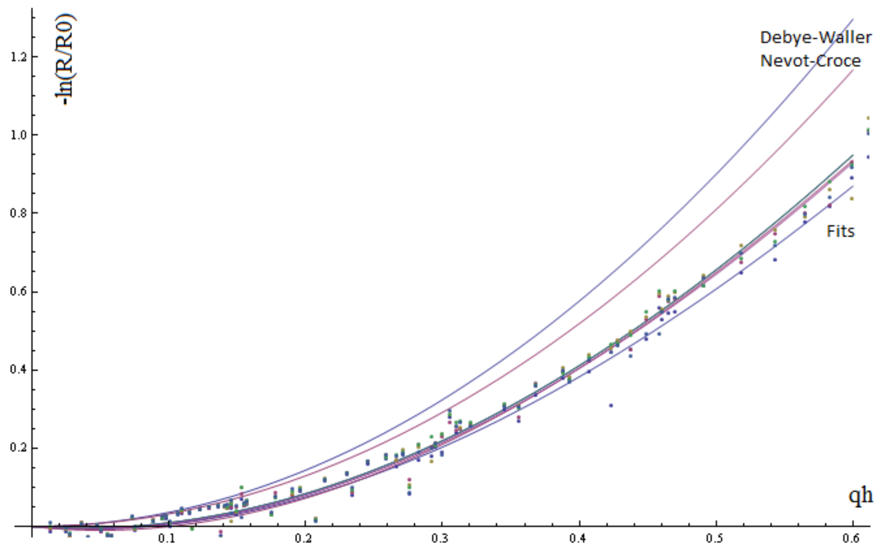

Figure 4.1 This figure compares the fits with the existing correction factors. The top to curves are the Debye-Waller and Nevot-Croce factors. The lower curves are the fits of the data for varying the frequency cut-off. There is a curve for each value of the cut-off as well as one for the aggregation of all data. The actual data is overlaid for comparison.

similar to Debye-Waller it exhibits smaller decreases in the reflection (see figure 4.1). In addition to having a quadratic term (whose coefficient is slight smaller) we have linear and cubic term which have the opposite sign of the quadratic term. This new correction to the reflectance will allow for improvements in XUV mirror design and fabrication.

4.2 Further Work

As we push forward the first order of business is finding the best solution to our ill-conditioned matrix. The most direct way through singular value decomposition. Rather than directly inverting the matrix decompositing it into a product of three matrices where the middle one is diagonal with the singular values. This allows one to detect and eliminate the problematic singular values and then solve by inverting each of these three matrices. While all of these matrices invert easily the decomposition is very costly, time wise. Another option is to combined the electric and magnetic

equations instead of solving the individually for the different polarizations. This is helpful because the ill-conditioned part of the matrix corresponds to strong resonant currents that do not radiate. Since these resonances happen in different places for the electric (equation 1.26) and magnetic (equation 1.27) fields, combining the equations allows the resonances to suppress each other. A third option is to use an iterative solution. This essentially works by guessing the answer, then plugging it in to see how far off it is. This is used to refine the guess and try again. Using physical optics we could get our intial guess close enough that this method could be faster then our current one. Also, iterative solutions can take advantage of special structure in the matrix and can be less sensitive to ill conditioned systems.

Once a suitable solution is found and implemented we will start looking at nonspecular reflection. With concerns about the accuracy of the AFM measurements [12], we desire a better way to measure the surface. With our computational model and the extreme small measurements we are capable of in the lab we feel that by measuring the nonspecular reflections we can determine learn about the surface. We should be able to find a relationship between the rms roughness and spatial frequency of the surface. This information can be used to adjust or recalibrate the AFM to give more accurate measurements of the surface.

Also the computational model makes no assumptions that limit its use to the XUV. It is derived generally in terms of wavelengths and can be used in problems across the whole EM spectrum.

Bibliography

[1] D. Allred, M. Squires, R. Turley, W. Cash, and A. Shipley, "Highly reflective Uranium mirrors for astrophysical applications," In *Proceedings of SPIE*, **4782,** 212–223 (2002).

[2] http://www.ssl.berkeley.edu/euve/sci/EUVE.html, 2001, (Accessed 4 August 2012).

[3] D. Attwood, *Soft X-rays and extreme ultraviolet radiation: principles and applications* (Cambridge University Press, 1999), p. Chapter 10.

[4] B. Sandel *et al.*, "The extreme ultraviolet imager investigation for the IMAGE mission," Space Science Reviews **91,** 197–242 (2000).

[5] IMAGE Mission EUV images available online at http://euv.lpl.arizona.edu/euv/, (Accessed 22 June 2012).

[6] U. Stamm, "Extreme ultraviolet light sources for use in semiconductor lithography-state of the art and future development," Journal of Physics D: Applied Physics **37,** 2344–3253 (2004).

[7] Y.-K. Choi and et al, J. Phys. Chem. B **107,** 3340–3343 (2003).

[8] A. Tritchkov, S. Jeong, and C. Kenyon, "Lithography Enabling for the 65 nm node gate layer patterning with alternating PSM," Proc. SPIE **5754,** 215–225 (2005).

[9] W. Chao, B. Hartenecx, J. Liddle, E. Anderson, and D. Attwood, "Soft X-ray microscopy at a spatial resolution better than 15 nm," Nature **435,** 1210–1213 (2005).

[10] K. Takemoto and et. al., "Transmission x-ray microscopy with 50 nm resolution in Ritsumeikan synchrotron radiation center," In *X-ray Microscopy AIP conference proceedings*, pp. 446–451 (1999).

[11] S. Lunt, Master's thesis, Brigham Young University, Provo, UT, 2000.

[12] N. Brimhall, Master's thesis, Brigham Young University, 2005, honors Thesis.

[13] J. Peatross and M. Ware, *Physics of Light and Optics* (Optics.byu.edu, 2011), (Accessed 23 July 2012).

[14] V. Holy, J. Kubena, and I. Ohlidal, Physical Review B **47,** 23 (1993).

[15] L. Nevot, B. Pardo, and J. Corno, Revue Phys. Appl. 23 (1988).

[16] P. Debye, verh. D. Deutsch. Phys. Ges **15,** 22 (1913).

[17] P. Croce and L. Nevot, J. De Physique Appliquee **11,** 5 (1976).

[18] D. de Boer, "Influence of the roughness profile on the specular reflectivity of x rays and neutrons," Physical Review B **49,** 9 (1994).

[19] A. Rockwood, undergrad. thesis (unpublished).

[20] S. Keller, undergard. thesis (unpublished).

[21] D. Stearns, "The Scattering of x rays from nonideal multilayer structures," Journal of Applied Physics **65(2),** 491–506 (1988).

[22] J. Johnson, Master's thesis, Brigham Young University, 2006.